Revista Mexicana de Astronomía y Astrofísica, 61, 189-203, (2025)

https://doi.org/10.22201/ia.01851101p.2025.61.03.07

Blade Antenna-SDR System Prototype for the CANTAR Global 21-cm Experiment: Simulations, Measurements, and In-Situ Results

Felipe P. Mosquera[1,4], **Julian Rodriguez-Ferreira** [1], **Efrén Acevedo** [1], **Oscar Restrepo** [2,4], **David González**[1] **and Germán Chaparro** [3,4]

[1]*Escuela de Ingenierías Eléctrica, Electrónica y Telecomunicaciones. Universidad Industrial de Santander, Universidad Industrial de Santander, Bucaramanga, Colombia.*
[2]*Universidad ECCI, Bogotá, Colombia.*
[3]*Grupo de Fisica y Astrofísica Computacional, FACOM, Universidad de Antioquia, Medellín, Colombia.*
[4]*Fundación para el Desarrollo de la Radioastronomía y Tecnologías Aplicadas - FUDARTA, Bogotá, Colombia.*

Keywords: *cosmology: observations, dark ages, reionization, first stars, instrumentation: detectors, instrumentation: miscellaneous, radio continuum: general, site testing*

Abstract

We present the design and initial testing of a low-frequency radio telescope prototype developed for the *Colombian Antarctic Telescope for 21-cm Absorption during Reionization* (CANTAR) experiment. Operating from 100 to 200 MHz, the system integrates a blade dipole antenna inspired by the EDGES high-band design with a software-defined radio (SDR) receiver. We report simulations of antenna impedance and beam chromaticity, along with SDR performance tests (Limenet Mini, Ettus E310, and USRP2920). A dual-stage low-noise amplifier reduces the system temperature, enabling foreground-sensitive observations. Radiometric estimates suggest that sub-mK sensitivity is achievable with 1000 h of integration. This prototype is part of Colombia's emerging infrastructure for 21-cm cosmology, with deployments planned at low-RFI sites in the Colombian Andes and Antarctica.

Resumen

Presentamos el diseño y pruebas de un prototipo de radiotelescopio de baja frecuencia para el experimento *Colombian Antarctic Telescope for 21-cm Absorption during Reionization* (CANTAR). El sistema opera entre 100 y 200 MHz, y combina una antena blade dipolo, inspirada en el diseño de *EDGES high-band*, con un receptor basado en un receptor de radio definido por software (SDR). Reportamos simulaciones de impedancia y cromaticidad del haz de la antena, junto con pruebas de desempeño de varios SDRs (Limenet Mini, Ettus E310, USRP2920). Un amplificador de bajo ruido de dos etapas reduce la temperatura del sistema, permitiendo observaciones sensibles a la emisión de fuentes del primer plano. Estimaciones radiométricas indican que es posible alcanzar sensibilidad de sub-mK con 1000 h de integración. Este prototipo es parte de la infraestructura emergente en Colombia para cosmología de 21 cm, con campañas planeadas en sitios de baja interferencia de radiofrecuencia (RFI) en los Andes Colombianos y la Antártida.

Corresponding author: Felipe P. Mosquera *E-mail address:* german.chaparro@udea.edu.co
Received: April 24, 2025 **Accepted:** August 25, 2025

---

1. Introduction

The redshifted 21-cm line of neutral hydrogen provides a unique observational window into the thermal and ionization histories of the early universe. In particular, measurements of the global (sky-averaged) 21-cm signal can probe the Cosmic Dawn and the Epoch of Reionization (EoR) (Barkana & Loeb, 2005; Furlanetto et al., 2006; Mozdzen et al., 2016). During this period, the first luminous sources coupled the hydrogen spin temperature to the kinetic temperature of the gas via the Wouthuysen-Field effect, producing an absorption signature in the 21-cm line against the cosmic microwave background (CMB) (Costa et al., 2018). The frequency range corresponding to this evolution lies between approximately 40 and 200MHz for redshifts $6 \leq z \leq 30$ (Bharadwaj & Ali, 2004), with an amplitude of ∼100–200mK and a width of ∼10MHz, depending on the astrophysical heating history.

This signal is embedded in a sky dominated by bright galactic synchrotron emissions and extragalactic foregrounds that are several orders of magnitude stronger ($\sim 10^3 - 10^4$ K). Its detection requires strict control over instrumental systematics, including beam chromaticity, impedance mismatches, and thermal gain variations (Bowman et al., 2009; Bernardi et al., 2016; Monsalve et al., 2017; Cheng et al., 2018; Restrepo et al., 2023). The controversial EDGES detection of an absorption feature at 78 MHz (Bowman et al., 2018), with an amplitude exceeding theoretical expectations, has renewed interest in independent validation and motivated a new generation of experiments (Monsalve et al., 2024).

Most global 21-cm efforts use single-element radiometers with fixed, analog backends. These include EDGES, SARAS (Singh et al., 2018), PRIZM (Philip et al., 2019), REACH (de Lera Acedo et al., 2022), BIGHORNS (Sokolowski et al., 2015). Although they differ in calibration approach, antenna type, and beam chromaticity control, they share the goal of suppressing the spectral structure in the instrument response. Interferometric arrays such as HERA (DeBoer et al., 2017), LEDA (Price et al., 2018), and LOFAR (Ghara et al., 2025) pursue complementary spatially resolved 21-cm measurements.

In this context, we present the design and initial testing of a modular low-frequency radio telescope prototype developed at the Universidad Industrial de Santander (UIS). The system combines a blade dipole antenna, modeled after the EDGES high-band design, with a reconfigurable software-defined radio (SDR) receiver chain (i.e., SDR based).

Unlike purpose-built analog backends, SDRs provide flexibility and rapid prototyping capabilities in radio science applications but raise concerns about spectral fidelity owing to the ADC resolution, phase noise, clock instability, and internal filtering (Feng et al., 2021; Ragoomundun & Beeharry, 2019; Keller et al., 2015). One aim of this study was to quantify these limitations and assess whether SDRs can serve as viable alternatives for radiometer-based 21-cm cosmology when combined with analog filtering and appropriate calibration strategies.

We also present electromagnetic simulations of the antenna, including S_{11} and beam chromaticity analyses, as well as in-situ measurements of the gain, sensitivity, and linearity for different SDR devices. We evaluated the dynamic range and noise temperature of the system under different preamplifier configurations and explored its response to controlled input signals. Although this prototype does not yet attempt sky signal extraction, it establishes a path toward future foreground characterization and calibration.

This prototype is the first instrument developed under the CANTAR initiative (Colombian Antarctic Telescope for 21-cm Absorption during Reionization), a long-term effort to design, test, and deploy low-frequency radiometers for global signal studies in low-RFI environments. CANTAR combines electromagnetic modeling and optimization with the development of novel analog and digital systems. It also features a robust Bayesian signal extraction and validation pipeline, as well as comprehensive site testing. Future deployments are planned for high-altitude locations in the Colombian Andes, as well as in Antarctica as part of the Programa Radioastronómico Antártico Colombiano (PRAC).

The remainder of this paper is organized as follows: §2 describes the system architecture, including the antenna design, SDR receiver configuration, and measurement setup. §3 presents the results from electromagnetic simulations, SDR performance tests, and in-situ measurements. In §4, we discuss the comparison between the simulations and measurements and assess the prototype's performance relative to other 21-cm experiments. §5 outlines future work and §6 summarizes our main findings and conclusions.

2. Methods

2.1. System Requirements

The design of the prototype system presented here is guided by constraints common to global 21-cm signal experiments, such as suppressing spectral structure in the system response and achieving wideband impedance matching. While the antenna does not require high spatial resolution, it must provide maximum gain at the zenith and maintain a return loss better than 10 dB, gain between 10-30 dB, and a noise figure below 4 dB (Restrepo et al., 2023). Table 1 summarizes the relevant characteristics of comparable global-signal experiments.

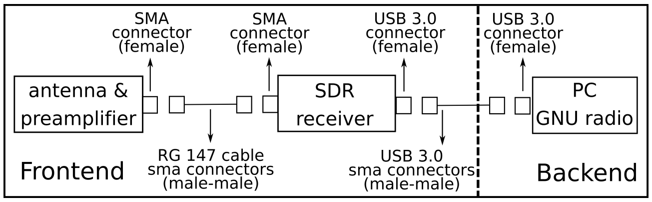

Figure 1. Subsystems of the radiotelescope to be validated.

At frequencies below 100 MHz, ionospheric refraction and absorption add further spectral complexity. These effects were not directly addressed in this study but must be accounted for in future long-duration deployments (Mora et al., in prep).

2.2. Role of SDR Technology

Software-defined radios (SDRs) provide a reconfigurable, low-cost backend with tunable sampling rates, bandwidths, and gain. Despite their widespread use in RFI monitoring and radiometry (Keller et al., 2015; Vacaliuc et al., 2011), SDRs remain underused in global 21-cm experiments because of their limited dynamic range, internal filtering stages, and susceptibility to quantization and clock drift artifacts.

In this study, we evaluated two commercially available SDRs, LimeNet Mini and Ettus E310, under conditions relevant to low-frequency radiometry. Both support open-source tools (GNU Radio, UHD) and are capable of tuning across the 100–200 MHz range. We assessed the suitability of each device through controlled signal injection, focusing on gain linearity, spectral flatness, and noise floor stability.

2.3. Radiotelescope System Description

Our prototype follows a modular design that combines a broadband blade dipole antenna, flexible analog front end, and SDR-based digital receiver. Although the antenna and ground plane geometry are inspired by the EDGES high-band system, our implementation introduces SDR-based signal processing and open-source data acquisition, allowing rapid reconfiguration and field deployment.

The system comprises three main subsystems: (1) a blade antenna mounted over a wire-mesh ground plane, (2) an analog front end including a balun and cascaded LNAs, and (3) a digital backend based on commercial SDRs, with acquisition scripts tailored for the platform in use. A system diagram is presented in Figure 1.

2.3.1. Antenna and Ground Plane

The antenna is a single-polarization blade dipole constructed from two aluminum plates mounted above a reflective ground plane. Its geometry is based on the high-band design used in the EDGES experiment, optimized for the 100–200 MHz frequency range following the Particle Swarm Optimization (PSO) scheme in (Restrepo et al., 2023). The dipole elements measure 62.5×48.1 cm and are positioned 52 cm above the ground, supported by a polystyrene structure chosen for its low dielectric constant and ease of fabrication (see Figure 2).

Table 1. Comparison between 21-cm cosmology experiments

System	Frequency range (MHz)	Antenna type	Use of balun	Calibration scheme
SARAS2	40-200	spheric monopole	no	coupled noise source
EDGES	100-200 50-100	blade	yes	antenna and noise source commutation
BIGHORNS	70-200	cone log-spiral	yes	antenna and reference source commutation
SCI-HI	40-130	hibiscus	yes	antenna, 50 and 100 Ohms loads and short terminal commutation
LEDA	40-85	double polarization dipole	yes	antenna and noise source commutation combined with cross-correlation of other antennas
MIST	40-125	blade dipole	yes	reference source calibration and soil calibration

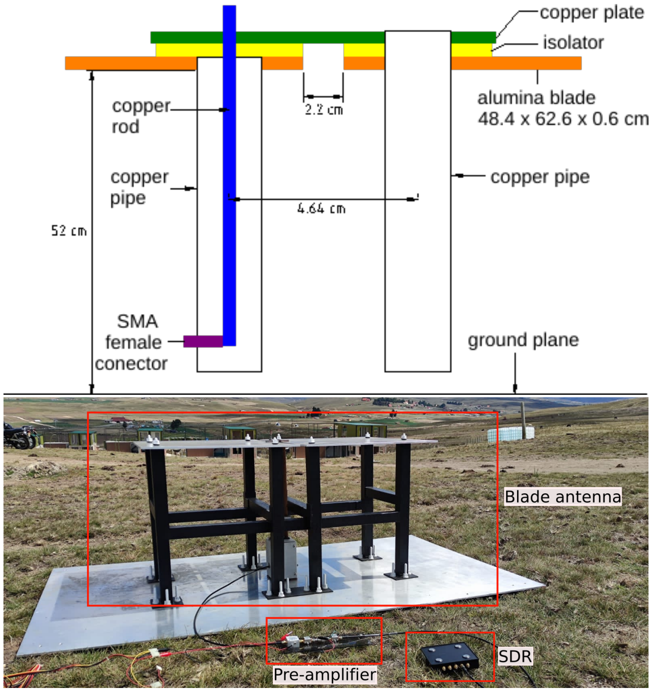

Figure 2. 100-200 MHz blade antenna. Schematic of the antenna (left), blade antenna in-situ at Páramo de Berlín (right).

The ground plane consisted of a central 1.3×1 m aluminum sheet, extended using wire mesh panels to a final area of 5×5 m. Although the initial simulations used only the solid plate, all measurements were performed with the fully extended plane, minimizing edge diffraction and reducing ground reflection systematics. Although this ground configuration is relatively modest compared to those used in experiments targeting precision spectral calibration, it represents a practical compromise for the prototyping phase.

A Roberts (or Collins) balun (Rogers, 2012) connects the balanced dipole to an unbalanced coaxial transmission line. This balun consists of two copper tubes and a sliding tuning plate, which allows for the mechanical adjustment of the electrical length and impedance match. The resonant frequency and bandwidth of the antenna can be shifted by varying the tuner height. A metal enclosure was added to suppress the common-mode currents along the feed structure. The output port is a standard SMA connector, which is located at the balun base.

2.3.2. Receiver Architecture and SDR Integration

The receiver chain is built around commercially available SDR hardware. The primary units evaluated in this study were the LimeNet Mini, Ettus E310, and USRP 2920. These were selected for their support of GNU Radio integration, capacity to digitize signals within the 100–200 MHz band, and configurability in terms of gain, bandwidth, and sampling parameters. Each SDR was tested under controlled signal injection to characterize its linearity, sensitivity and spectral response.

The analog front end includes one or two stages of low-noise amplification, depending on the configuration, with optional filtering. The tests were performed using commercially available mini-circuit LNAs (ZX60-P103LN+) and bias tees. Additional filtering stages are being developed to reduce the out-of-band RFI and suppress the system gain variation near the band edges. Different gain settings were explored to assess the interplay between the amplifier noise temperature, SDR quantization effects, and system linearity.

2.4. Signal Processing and Software Architecture

The digital processing pipeline was implemented using the GNU Radio. A base flow graph was constructed using SDR source blocks, configurable gain and bandwidth parameters, and a file sink for raw data output. Each acquisition consists of a set of overlapping frequency windows, each spanning 16 MHz, stitched together to cover the full 100–212 MHz band. The overlap between adjacent windows allows for the detection and removal of edge artifacts owing to digital filtering.

Python scripts were written to parse the raw binary output, assign frequencies, and construct the power spectra for each band segment. The software supports flexible gain-averaging and FFT configurations. Optional real-time smoothing using Savitzky–Golay filters was implemented as a testbed for future

RFI rejection and dynamic compression strategies. Although data processing was performed offline for the results presented here, the pipeline supports near-real-time visualization, which is useful for system monitoring and on-site deployment.

Preliminary data are stored in structured directories organized by the acquisition date and SDR type. The system is compatible with both Linux-based embedded platforms (as in the case of Ettus E310 and LimeNet Mini) and external laptops interfaced via USB or Ethernet. All acquisition routines were designed to be portable and easily adapted to other SDR models or front-end configurations[1].

Two software packages were built, one for use with the Limenet mini (`lime_eor`) and the other for the Ettus E310 (`etus_eor`). Each main folder contains the same file structure but is configured for each SDR separately. Taking the Ettus folder as an example, it contains three files with `.py` extension and two folders, *"data"* and *"graphics"*.

The data acquisition and processing workflow relies on a set of Python scripts developed around the flowgraph outputs of GNU Radio. Figure 3 shows a diagram of the software architecture implemented. Three main scripts structure the pipeline.

- `python_graficas_2.py` is an auto-generated script produced by the GNU Radio based on the implemented flowgraph. It defines the SDR configuration, sampling parameters, and data sinks for the binary output.
- `dataGNU.py` processes the binary output produced by the SDR. It extracts the center frequency (typically 108 MHz) and defines the sampling rate (16 MS/s), resulting in a 16 MHz display bandwidth with an FFT size of 6144. The script parses the raw `.bin` file using `numpy`, reshapes the data into power spectra, and generates frequency-calibrated plots. The frequency axes, power scaling, and display parameters were set programmatically, enabling batch visualization of the spectral segments.
- `tomaDatosRFI.py` automates the full-band acquisition by iterating over six center frequencies to cover the 100–212 MHz range in overlapping 16 MHz windows. For each window, the script generated spectrum plots and stored them in timestamped subdirectories. It also creates a `.txt` file containing the raw numerical data for post-processing. At the end of each run, the center frequency was reset to 108 MHz to ensure consistency. A companion script, `multiplesTomasRFI.py`, allows repeated acquisitions over configurable time intervals to monitor RFI variability.

2.5. Antenna simulations

We performed electromagnetic simulations of the antenna using Ansys HFSS to characterize its reflection coefficient (S_{11}) and beam chromaticity across the 100–200 MHz band. The model geometry matched the constructed blade dipole described in the previous section, including the feed gap, plate dimensions, and elevation above the ground. Chromaticity was evaluated in the principal planes $\phi = 0°$ and $\phi = 90°$, which is consistent with the expected sky coverage.

To reduce computational complexity, the simulated ground plane was limited to the central 1.3 m × 1.0 m aluminum sheet, excluding the full 5 m × 5 m wire mesh used in the physical system. This simplification may introduce minor discrepancies in the low-frequency edge of the band, where the extent of the ground plane has a greater impact on the impedance and beam structure.

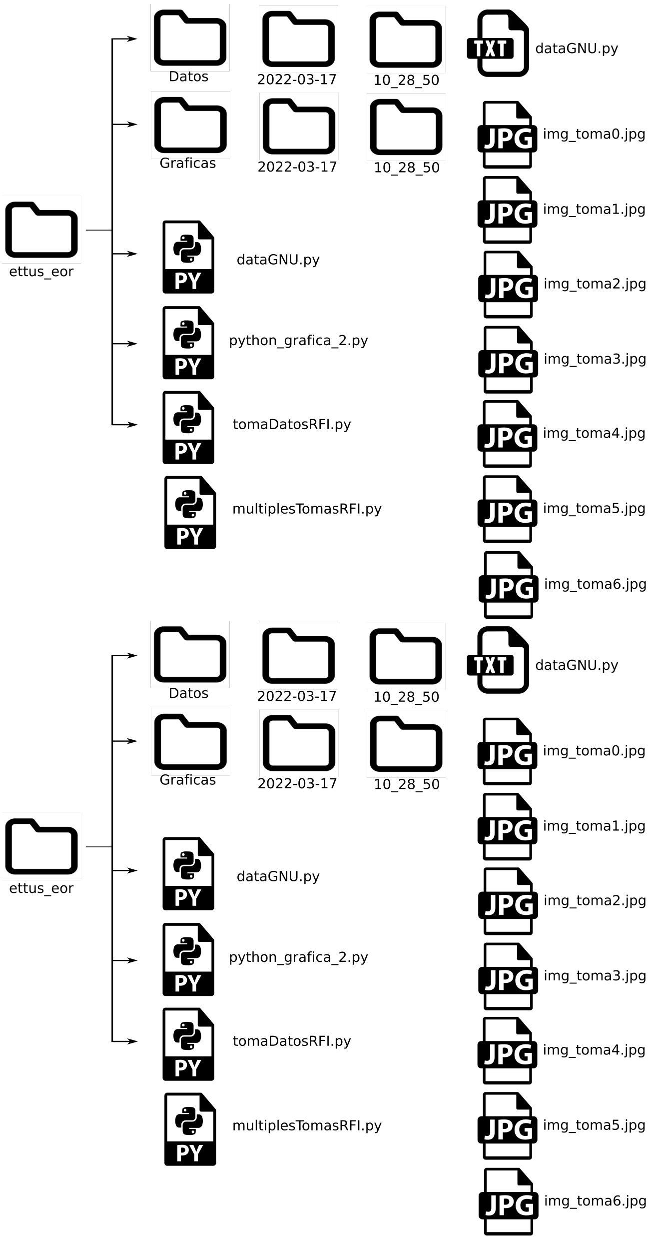

Figure 3. Software architecture using GNU Radio.

Simulations were used to guide balun tuner optimization and establish baseline expectations for matching and spectral smoothness, informing both mechanical construction and post-fabrication calibration strategies.

3. Results

This section presents the system-level performance metrics derived from the simulated and measured components, including the antenna S-parameters, chromaticity, effective antenna area, source brightness temperature, and total system noise temperature under various preamplifier configurations. We also present the experimental validation of the antenna and receiver subsystems, including in situ measurements of the antenna impedance response, laboratory tests of SDR performance, and gain characterization of the low-noise amplifiers (LNAs). Finally,

---

[1] The algorithms were developed by Ronal Sebastian Buitrago Parra, Yeison Andrés Quiroga Malambo, Brayan Nicolas Suarez Mongui, and Felipe P. Mosquera.

Table 2. Blade antenna S_{11} parameter simulation results

Quantity	7.5 cm	12.5 cm	22.5 cm	32.5 cm	45.5 cm
Minimum frequency @-10dB (MHz)	100	100	100	100	145
Maximum frequency @-10dB (MHz)	147	150	157	170	200
Bandwidth (BW) (MHz)	447	50	57	70	55
Minimum gain (dB)	-16.85	-17.98	-21.25	-28.54	-27.24
Frequency @ min. gain (MHz)	122	123	130	139	169

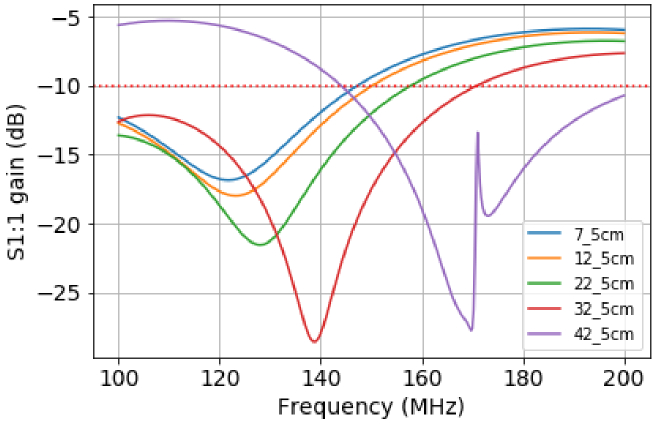

Figure 4. S_{11} simulations for the blade antenna considering 5 balun heights.

we evaluated the response of the SDR receivers in terms of linearity and noise levels.

3.1. S_{11} Response

The reflection coefficient S_{11} was simulated for five different balun tuner heights by varying the effective electrical length of the antenna feed. These heights, ranging from 7.5 to 42.5 cm above the balun base, were selected to explore the tuning effects across the 100–200 MHz band (see Table 2). The frequency range where $S_{11} < -10$ dB was considered the operational bandwidth in each case. Figure 4 illustrates the behavior of the blade antenna as it iterates between different balun tuner heights.

The results show that lower balun heights favor a flatter response near 100 MHz, whereas higher heights shift the resonance toward the upper band edge. The widest matched bandwidth was obtained at 32.5 cm, with $S_{11} < -10$ dB across 100–170 MHz. The peak reflection minima reached values below -25 dB in several configurations, indicating a good impedance match in those regions. These trends informed the selection of the tuner heights during the measurements (see § 5).

3.2. Beam Chromaticity

To assess the beam chromaticity, far-field gain patterns were simulated as a function of frequency at a fixed balun height of 22.5 cm. Cuts at $\phi = 0°$ and $\phi = 90°$ were extracted over the 100–200 MHz range. The results of the chromaticity simulations for the blade antenna (with balun) are shown in Figure 5. The chromatic response was characterized by tracking the gain variation at each elevation angle as a function of the frequency and calculating the differential gain relative to a fixed reference frequency.

In both planes, the antenna exhibited reduced chromatic variation at the zenith and increased variation near the horizon, as expected. For $\phi = 0°$, the gain variation below 20° elevation exceeds 3 dB over the band, whereas at higher elevations, it remains relatively flat. For $\phi = 90°$, the behavior is broadly similar, with the smoothest region occurring between 60° and the zenith. These results are consistent with the expectations for a blade dipole and suggest that the antenna is sufficiently stable for beam modeling and calibration, especially if zenith-pointing observations are prioritized (Restrepo et al., 2023).

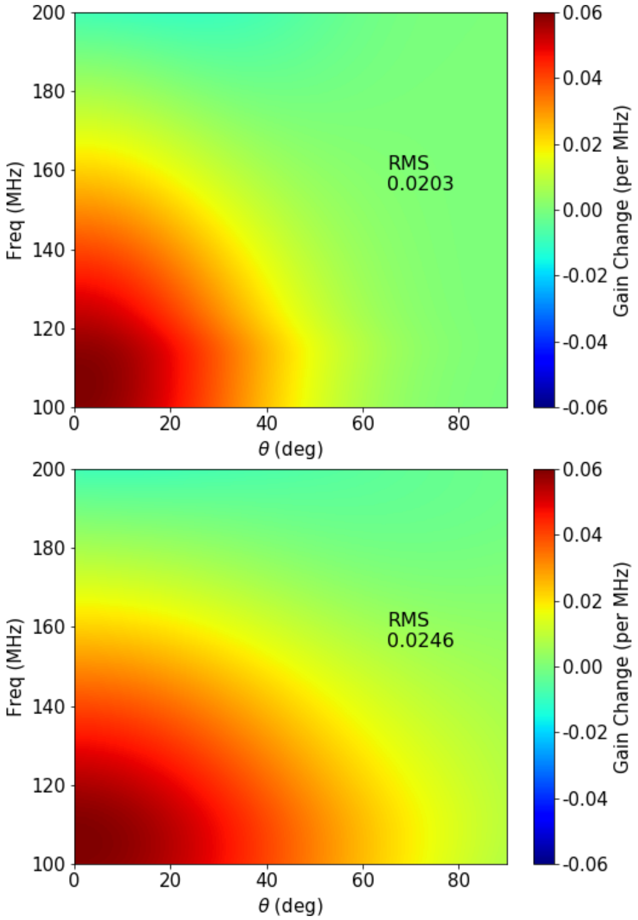

Figure 5. Blade antenna chromaticity simulation for a balun height @ 22.5 cm. Gain change for the $\phi = 0°$ (left) and $\phi = 90°$ (right) planes.

Table 3 summarizes the simulated bandwidth and reflection minima for each balun tuner height. Although the simulations neglect ground screen extensions and lossy soil effects, they provide a useful reference for interpreting the measured response and guiding balun adjustments during field deployment.

3.3. System Characterization Measurements

We conducted system characterization measurements to quantify the system behavior across the 100–200 MHz band and identify

Table 3. Simulated S_{11} parameters for different balun heights

Parameter	7.5 cm	12.5 cm	22.5 cm	32.5 cm	42.5 cm
Min freq. @ S_{11} <-10 dB (MHz)	100	100	100	100	145
Max freq. @ S_{11} <-10 dB (MHz)	147	150	157	170	200
Bandwidth (MHz)	47	50	57	70	55
Min S_{11} (dB)	−16.85	−17.98	−21.25	−28.54	−27.24
Freq. @ Min S_{11} (MHz)	122	123	130	139	169

Table 4. Measured S_{11} parameters for different balun tuner heights

Parameter	7.5 cm	12.5 cm	22.5 cm	32.5 cm	45.5 cm
Min freq. @ $S_{11} < -10$ dB (MHz)	112	112	111	111	117
Max freq. @ $S_{11} < -10$ dB (MHz)	145	149	158	166	179
Bandwidth (MHz)	33	37	47	55	62
Min S_{11} (dB)	−15.81	−16.50	−19.72	−41.91	−28.45
Freq. @ Min S_{11} (MHz)	126	124	124	126	161

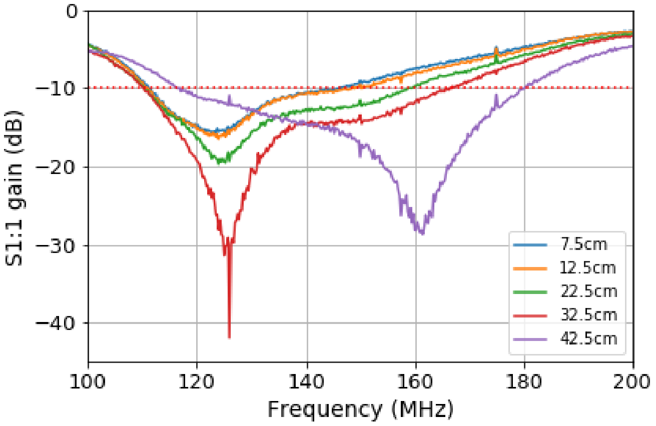

Figure 6. S_{11} VNA measurements considering different balun tuner heights.

configurations that minimize instrumental contributions to the overall system temperature.

3.3.1. Antenna Reflection Measurements

The antenna reflection coefficient S_{11} was measured on-site at the Páramo de Berlín using a Keysight FieldFox N9914A vector network analyzer (VNA) operating from 30 kHz to 6.5 GHz. As in the simulations, five balun tuner heights were tested to evaluate the impact of the electrical length on the impedance match. Figure 2 shows the antenna design.

Figure 6 shows the measured S_{11} curves for the different balun heights. The results are summarized in Table 4, which includes the matched frequency range ($S_{11} < -10$ dB), total bandwidth, minimum reflection, and the frequency of minimum return loss.

The measured bandwidths and reflection minima showed good agreement with the HFSS simulations, with minor shifts attributable to the real ground conditions and the extended mesh ground plane not included in the simulation model. The deepest match was achieved at 32.5 cm, which is consistent with the simulation predictions.

3.3.2. SDR Linearity and Sensitivity

To evaluate the dynamic range and sensitivity of the SDR receivers, we performed controlled signal injection tests using a calibrated RF signal generator (Marconi 2023A, maximum additional uncertainty in standard configuration: 0.5 dB) and a spectrum analyzer (R&S ZVL6) (level measurement uncertainty: <0.5 dB). Figure 7 shows the SDR measurement setup. Three SDRs were tested: LimeNet Mini, Ettus E310, and USRP 2920. Two measurement sets were conducted: one probing linearity across frequency at a fixed input power and another probing sensitivity at a fixed frequency with varying input levels.

For the linearity test, a −30 dBm tone was swept from 100 to 200 MHz in 1 MHz steps. The SDRs were configured with zero gain to reflect the default field operation. All devices exhibited a monotonic response across the band, although with different overall gain scalings. The Ettus E310 showed the most stable and consistent output, whereas the LimeNet Mini exhibited higher variability and a significantly elevated noise floor.

For sensitivity, a 150 MHz tone was injected at power levels ranging from −30 to −130 dBm. Each SDR was tested across gain settings from 0 to 60 dB. The LimeNet Mini showed detection thresholds of approximately −60 dBm at 0 dB gain, improving to approximately −90 dBm at 30 dB. The E310 demonstrated lower detection thresholds across the board, reliably detecting signals as low as −110 dBm at moderate gain settings. The USRP 2920 offered the best raw sensitivity but exhibited compression artifacts at a high gain. Figure 9 shows the results.

These results indicate that although all three SDRs are suitable for exploratory measurements, careful gain calibration and noise floor characterization are essential, especially when seeking stability at millikelvin scales.

3.3.3. LNA Gain Characterization

The analog front-end amplification chain employs mini-circuit ZX60-P103LN+ LNAs. To quantify the gain and spectral flatness, we measured the forward transmission parameter (S_{21}) of both the single and cascaded LNA configurations using the FieldFox VNA. Figure 10 shows the LNA response (level measurement uncertainty: <0.5 dB).

A single amplifier exhibited a flat gain of approximately 24.5 dB from 50 to 100 MHz, decreasing gradually to 23.0 dB at 200 MHz.

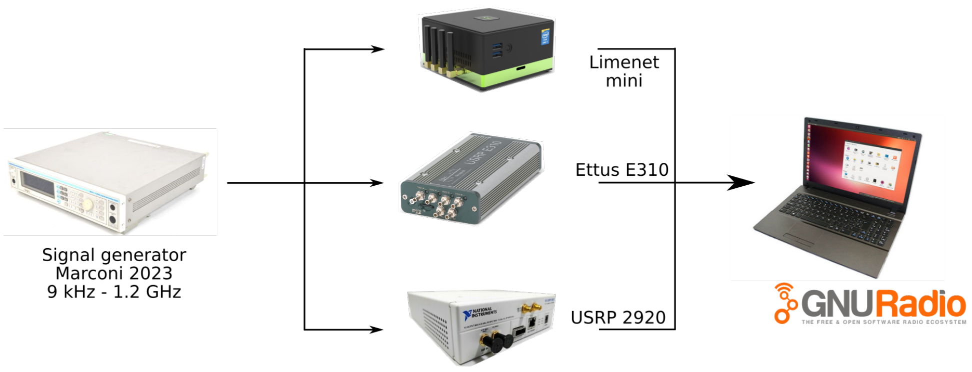

Figure 7. Setup for SDR measurements.

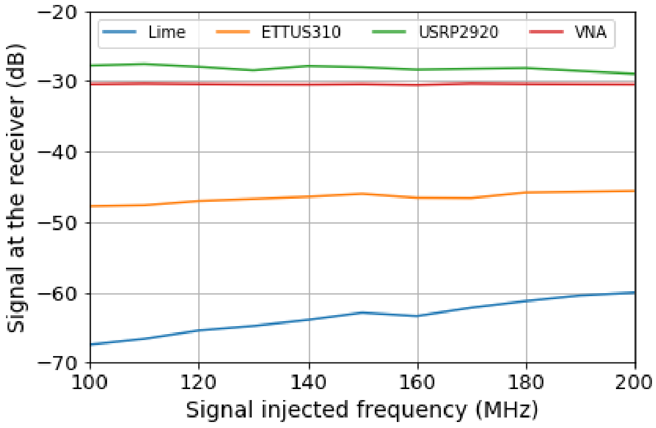

Figure 8. SDRs linearity response. Limenet mini, Ettus E310 and USRP2920 linearity response @ gain=0, injecting -30 dBm and varying the frequency between 100 and 200 MHz.

The cascaded pair delivered a combined gain of 49.5 dB at 100 MHz, tapering to approximately 47.6 dB at 200 MHz. This decline reflects the specified performance and is consistent with the manufacturer's datasheet.

The measurements confirmed that the amplifier stages introduced a minimal spectral structure over the band of interest and were suitable for use with moderate-gain SDRs. However, future configurations will incorporate bandpass filters to suppress out-of-band noise and mitigate gain compression near strong RFI sources.

3.4. Antenna performance metrics

3.4.1. Effective Area and Source Temperature

The antenna gain was estimated from HFSS simulations to be approximately 7 dBi at the zenith near 150 MHz, corresponding to a linear gain of $G = 5.01$. The effective area A_{e} at this frequency is given by

$$A_{\mathrm{e}} = \frac{\lambda^2 G}{4\pi} = \frac{(2\,\mathrm{m})^2 \cdot 5.01}{4\pi} \approx 1.59\ \mathrm{m}^2, \tag{1}$$

where $\lambda = c/\nu$ is the wavelength at 150 MHz.

To estimate the system response to a strong known radio source, we considered the quiet Sun, which has a flux density of 1.24×10^6 Jy at 150 MHz. The corresponding antenna temperature is

$$T_{\mathrm{src}} = \frac{A_{\mathrm{e}}}{2k} \cdot S = \frac{1.59}{2k} \cdot 1.24 \times 10^{-20}\ \mathrm{W\,m^{-2}\,Hz^{-1}} \approx 716\ \mathrm{K}. \tag{2}$$

This value provides a consistency check for the radiometric calibration and detection threshold estimates.

3.4.2. System Temperature Estimates

We estimated the total system temperature T_{sys} under three scenarios: (1) without a preamplifier, (2) using the current preamplifier (two cascaded ZX60-P103LN+ amplifiers), and (3) using the proposed preamplifier chain, including filtering stages. The Friis equation was used to compute the equivalent noise temperature of the system, incorporating the cable losses, amplifier gains, and manufacturer-specified noise figures.

In all cases, the antenna temperature was assumed to be $T_{\mathrm{ant}} =$ 300 K, based on ITU-R P.372-7, and accounting for both galactic noise and moderate terrestrial RFI contributions at 200 MHz.

3.4.3. System Behavior without Preamplifier

Without any preamplification, the signal is passed through 30 m of LMR400 coaxial cable (~1.5 dB loss) to the SDR receiver. Figure 11 illustrates a conceptual diagram of the subsystems used to calculate the overall temperature of the system. In this case, no preamplifier was considered. To determine the system temperature without a preamplifier, we considered the contributions of both the cable and receiver. The 100-foot LMR400 cable exhibited a gain of -1.5 dB (linear gain of 0.993), noise figure of 1.5 dB, and temperature of 119.36 K. The Ettus E310 receiver had a noise figure of 8 dB and a temperature of 1539.776 K. For an Ettus E310 receiver with an 8 dB noise figure, the total system temperature is

$$T_{\mathrm{sys}} = T_{\mathrm{ant}} + T_{\mathrm{rx}} \approx 300\ \mathrm{K} + 1370\ \mathrm{K} = 1670\ \mathrm{K}, \tag{3}$$

indicating that cable attenuation and receiver noise were dominant in this configuration.

Table 5 presents the results of the calculations for the system, considering that T_{REF} is the temperature of the receiver (all stages except the antenna), T_{ANT} is the temperature of the antenna, T_{SYS} is the temperature of the system, NF is the noise figure, and F is the noise factor.

3.4.4. System Behavior With Current Preamplifier

The existing analog front end includes two cascaded ZX60-P103LN+ amplifiers (each with 23 dB gain and 1.2 dB NF), along with bias tees and short interconnects. Figure 12 presents a schematic of the current preamplifier stages, and Table 6 lists the following parameters: component model, gain (linear and in dB), noise figure (dB), and temperature (K). By accounting for the cable loss and gain distribution, the estimated system temperature was significantly reduced:

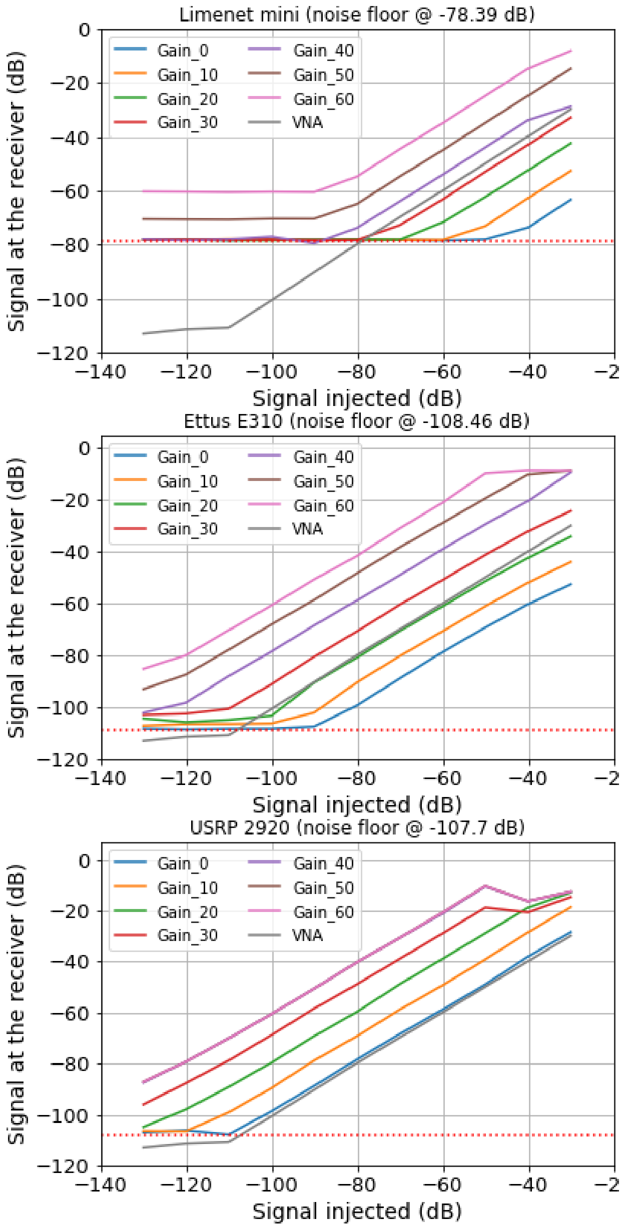

Figure 9. SDRs sensitivity response. Limenet mini (top-left), Ettus E310 (top-right) and USRP2920 (bottom) sensitivity response @ SDR gain = 0, injecting 150 MHz and varying the RF level between −30 and −120 dBm.

Table 5. System temperature and noise figure results (without pre-amplifier)

Parameter	Value
Antenna Effective area	1.5947 m^2
Source temperature (Sun)	716.459 K
T_{RX}	1669.99 K
T_{ANT}	300 K
T_{SYS}	1969.99 K
NF	8.917 dB
F	7.79

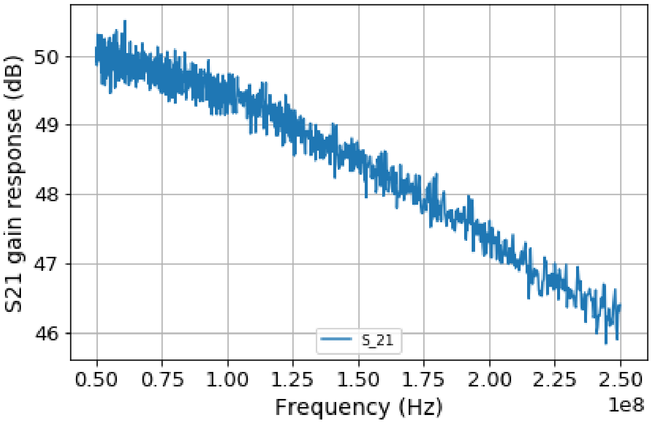

Figure 10. Pre-amplifiers LNA S_{21} response. S_{21} response of the current pre-amplifier LNA ZX60-P103LN+, testing one LNA (top) and testing two-serial LNAs (bottom).

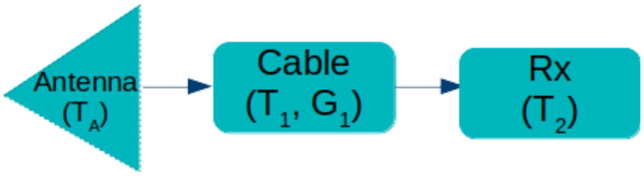

Figure 11. Front-end block diagram (without pre-amplifier).

$$T_{\text{sys}} \approx 300\text{ K} + 153\text{ K} = 453\text{ K}, \tag{4}$$

with an equivalent noise figure of approximately 4.1 dB.

Table 7 presents the results for the current preamplifier in terms of T_{RX}, T_{ANT}, T_{SYS}, NF, and F.

3.4.5. System Behavior With Proposed Filtered Preamplifier

The proposed configuration adds high- and low-pass filters to suppress the out-of-band power and improve the gain flatness. Two ZX60-33LNR-S+ amplifiers, each with 24.7 dB gain and 1.1 dB NF, were combined with Mini-Circuits filters SHP-20+ and SLP-250+. These filters restrict the frequencies adjacent to those of interest (between 100 and 200 MHz) (see Figure. 13). This architecture is based on the preamplification stage used in the MIST and MINI-MIST projects (Restrepo et al., 2020). The resulting system temperature is further reduced as follows:

$$T_{\text{sys}} \approx 300\text{ K} + 143\text{ K} = 443\text{ K}, \tag{5}$$

with an overall noise figure of 4.0 dB. This improvement is modest in absolute terms but is important for achieving a higher dynamic range and minimizing foreground leakage in the final power spectrum. The values obtained for the system temperature estimation parameters are listed in Table 8. Table 7 lists the results of the calculations of the system temperature using a preamplifier.

3.5. SDR Sensitivity and Linearity Comparison

Three SDR receivers were evaluated using signal injection tests: LimeNet Mini, Ettus E310, and USRP 2920. Each device exhibited distinct noise floors and gain characteristics, largely owing to differences in the ADC architecture and internal filtering. Figure 14 shows the response of each device to a fixed 150 MHz tone at varying RF input levels, measured at receiver gain settings of 0 dB and 30 dB.

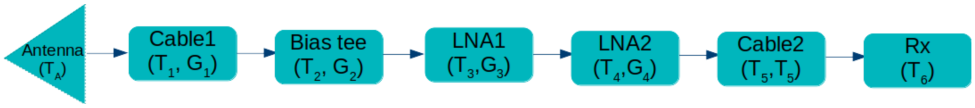

Figure 12. Front-end block diagram (current pre-amplifier).

Table 6. System temperature estimation parameters (current pre-amplifier)

Component	Reference	G	G	NF	T
		(dB)	(linear)	(dB)	(K)
Cable1 (T_1, G_1)	086-2SM+ × 2 in	-0.03	0.993	0.03	2.01
Bias tee (T_2, G_2)	ZFBT-4R2GW-FT	-0.6	0.871	0.6	42.96
LNA1 (T_3, G_3)	ZX60-P103LN+	23	199.526	1.2	92.92
LNA2 (T_4, G_4)	ZX60-P103LN+	23	199.526	1.2	92.92
Cable3 (T_5, G_5)	LMR400 ×100 ft	-1.5	0.993	1.5	119.36
Receiver (T_6)	Ettus E310	–	–	8	1539.776

Table 7. System temperature and noise figure results (current pre-amplifier)

Parameter	Value
Antenna Effective area	1.5947 m^2
Source temperature (sun)	716.459 K
T_{RX}	153.27 K
T_{ANT}	300 K
T_{SYS}	453.27 K
NF	4.09 dB
F	2.56

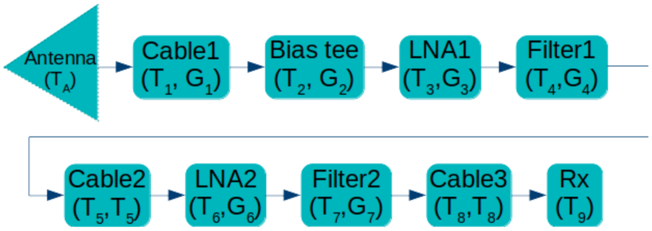

Figure 13. Front-end block diagram (proposed preamplifier).

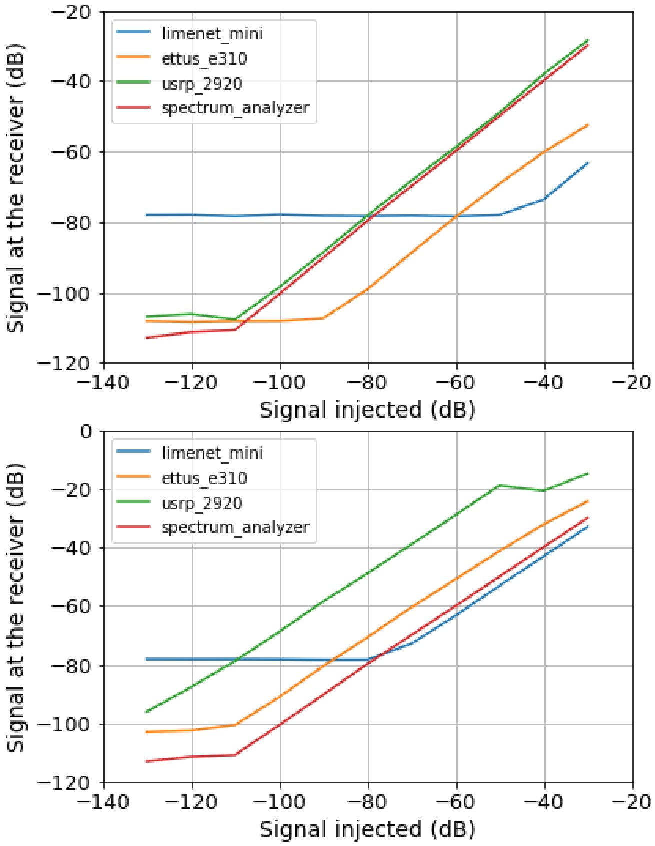

Figure 14. SDRs sensitivity comparison: Limenet mini, Ettus E310 and USRP2920 @ gain = 0 dB (left) and @ gain = 30 dB (right), injecting 150 MHz and varying the RF level between −30 and −120 dBm.

The Ettus E310 exhibited the lowest noise floor (−108.5 dB) and most linear response, closely matching the reference spectrum analyzer. The USRP 2920 performed comparably in terms of sensitivity but showed an early onset of gain compression. Although functional, LimeNet Mini had a significantly higher noise floor (−78 dB) and poorer spectral stability.

The optimal operating gain for each SDR was determined by sweeping the gain settings from 0 to 60 dB. For LimeNet, the best tradeoff between distortion and sensitivity occurred at 30 dB; for E310, it was 20 dB; and for USRP, 0 dB. These values provide guidance for system configuration during sky measurements and influence the preamplifier design, particularly for minimizing the total system temperature.

Tests involving fixed RF power and swept frequency confirmed that the USRP 2920 delivered the most spectrally flat and consistent output, particularly at high input levels. The E310 showed slightly more variation but maintained an acceptable linearity.

3.6. System Integration and In-Situ Measurements

The complete system (antenna, transmission line, preamplifier, and SDR) was deployed for initial sky testing at the Páramo de Berlín location. The preamplifier followed the configuration discussed above, and the Ettus E310 was used as the receiver, which was configured with a 0 dB gain. The software setup, including the FFT and averaging parameters, followed the definitions in § 3.3.

Table 8. System temperature estimation parameters (proposed preamplifier)

Component	**Reference**	G (dB)	G (linear)	NF**)** (dB)	T (K)
Cable1 (T_1, G_1)	086-2SM+ × 2 in	-0.03	0.993	0.03	2.01
Bias tee (T_2, G_2)	ZFBT-4R2GW-FT	-0.6	0.871	0.6	42.96
LNA1 (T_3, G_3)	ZX60-33LNR-S+	24.7	295.121	1.1	83.592
Filter1 (T_4, G_4)	SHP-20+	-0.13	0.971	0.13	8.812
Cable2 (T_5, G_5)	086-2SM+ × 2 in	-0.03	0.993	0.03	2.01
LNA2 (T_6, G_6)	ZX60-33LNR-S+	24.7	295.121	1.1	83.592
Filter2 (T_7, G_7)	SLP-250+	-0.27	0.94	0.27	18.601
Cable3 (T_8, G_8)	LMR400 ×100ft	-1.5	0.993	1.5	119.36
Receiver (T_9)	Ettus E310	–	–	8	1539.776

Table 9. System temperature and noise figure results (proposed preamplifier)

Parameter	**Value**
Antenna Effective area	1.5947 m^2
Source temperature (sun)	716.459 K
T_{RX}	143.32 K
T_{ANT}	300 K
T_{SYS}	443.32 K
NF	4.02 dB
F	2.53

Figure 15 shows the measured spectra across the full 100–212 MHz band, segmented into seven overlapping 16 MHz windows. The response followed the expectations based on the previous component-level tests. The signal and noise are amplified together, underscoring the need for filtering stages to suppress out-of-band contributions.

To explore real-time data processing, we implemented a Savitzky–Golay filter with three levels of averaging. Figure 16 shows the filtered spectra with low (9-point polynomial), medium (6-point), and high (3-point) smoothing. Although computationally intensive, such averaging is useful for reducing the data volume and identifying persistent spectral features in near-real time.

Each full-band acquisition, including the averaged and unaveraged spectra and raw data files, required approximately 52.6 MB of storage. This metric informs future hardware and data management planning, especially as the system evolves toward longer integration times and field campaigns in the future.

As a supplementary outcome of the project, six bilingual technical manuals were created. These include guides for VNA calibration, dipole simulation in HFSS, and blade-antennas modeling. The documentation is stored on the internal servers of the Universidad Industrial de Santander Research Groups E3T and RadioGIS for institutional access and training purposes.

4. Discussion

4.1. Implications for Sky Measurements

The system temperature values in Table 10 set practical limits on the sensitivity of drift-scan observations. For integration times of several hours and moderate sky averaging, a noise floor of a few kelvin root mean square (RMS) per megahertz (MHz) bin is expected. While this is far from the 10–100 mK target required for the direct detection of the global 21-cm signal, it is sufficient for characterizing the foreground structure, verifying instrument stability, and developing calibration techniques.

Further reduction of the system temperature would require either cryogenic front-end amplification or the use of differential radiometric techniques. These system temperature values (see Table 11) set practical limits on the sensitivity of drift-scan observations. For the integration times estimated below, a noise floor of a few kelvin RMS per MHz bin is expected to be achieved. Although this is far from the 10–100 mK target required for the direct detection of the global 21-cm signal, it is sufficient for characterizing the foreground structure, verifying instrument stability, and developing calibration techniques before the next stage of observations with optimized antennas.

4.2. Radiometric Sensitivity and Detection Thresholds

To assess the theoretical sensitivity of the system in the context of global 21-cm signal detection, we applied the radiometer equation:

$$\Delta T = \frac{T_{\mathrm{sys}}}{\sqrt{B\,t}}, \tag{6}$$

where ΔT is the RMS thermal noise, T_{sys} is the system temperature, B is the bandwidth, and t is the integration time. Using the best-performing configuration described in § 6, we adopted a measured system temperature of $T_{\mathrm{sys}} \approx 443$ K, which is representative of the filtered dual-stage preamplifier design.

Assuming a bandwidth of 1 MHz is sufficient to resolve the broad absorption feature predicted for the global 21-cm signal—and a total integration time of 1000 hr, the thermal noise limit is

$$\Delta T = \frac{443}{\sqrt{10^6 \times 3.6 \times 10^6}} \approx 0.23 \text{ mK}. \tag{7}$$

This result indicates that, under ideal observation conditions and assuming perfect calibration and system stability, the instrument is thermally capable of detecting signals at the sub-millikelvin level. Because the anticipated global 21-cm signal during the Cosmic Dawn has an amplitude on the order of 100 mK, the current system, at least from a thermal noise perspective, is sufficiently sensitive. For comparison, the HERA experiment used a similar integration time of 94 nights to place stringent upper limits on the 21 cm power spectrum during reionization,

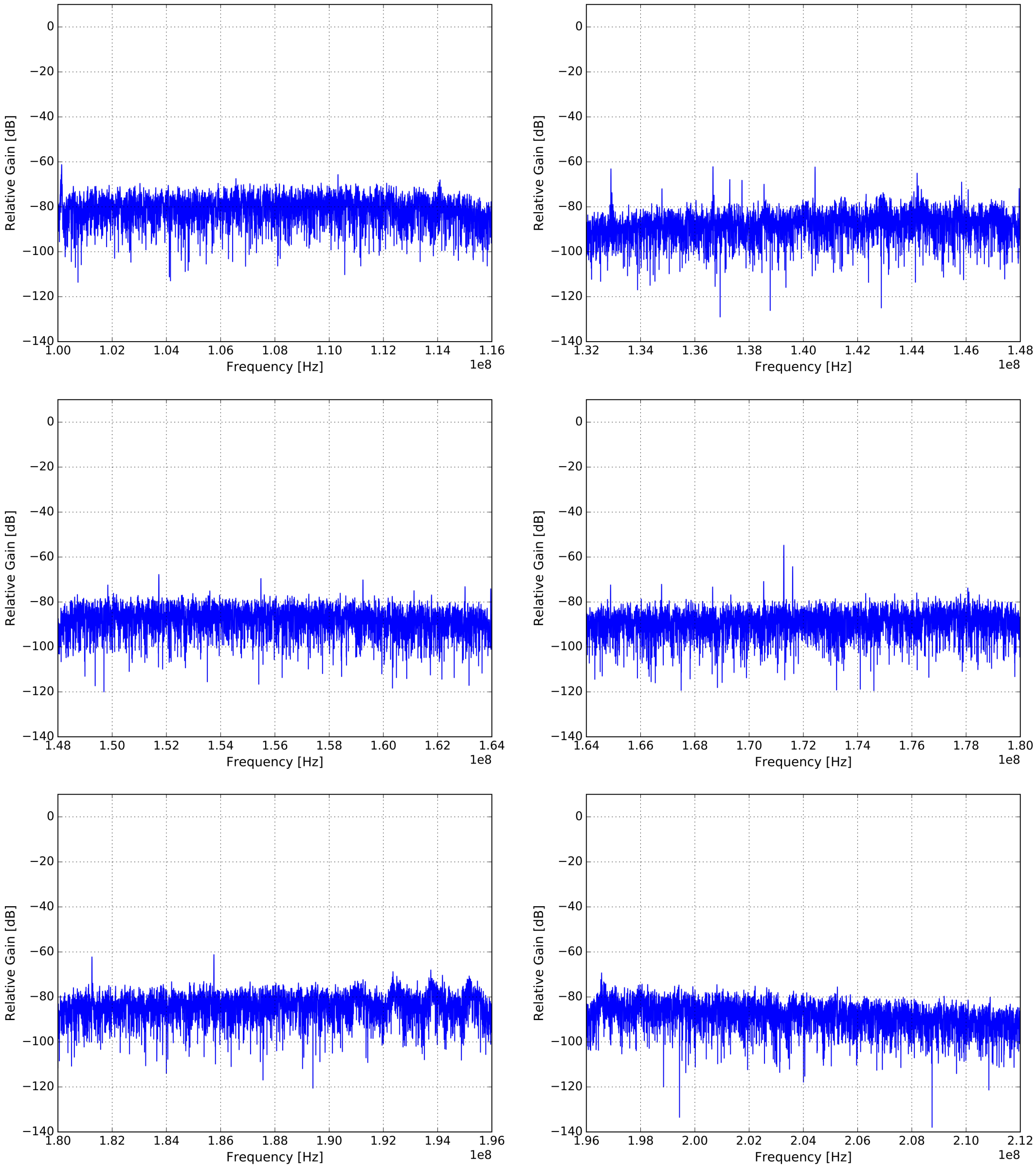

Figure 15. In-situ RFI measurements considering the following frequency ranges: 100-116 MHz, 132-148 MHz, 148-164 MHz, 164-180 MHz, 180-196 MHz and 196-212 MHz. The 116-132 MHz measurements are presented in the following figure.

Table 10. Summary of system temperature and noise performance for three receiver configurations

Configuration	T_{SYS} (K)	NF (dB)	F (linear) (linear)
No preamplifier	1670	8.9	7.79
Current preamplifier	453	4.1	2.56
Filtered preamplifier	443	4.0	2.53

reaching sensitivities sufficient to rule out a broad class of cold IGM models (Facchinetti et al., 2024).

However, practical detection of the 21-cm signal requires suppression of instrumental systematics and astrophysical foregrounds to below the ∼10 mK level. In this context, beam chromaticity, gain instability, and calibration drift are the dominant challenges. Achieving effective signal recovery will require robust absolute calibration schemes, improved spectral smoothness, and potentially differencing or switching techniques to isolate the sky signal from the instrumental response.

The present sensitivity benchmark demonstrates that the system is capable of contributing to foreground characterization and site stability studies and may serve as a viable platform for future calibrated global signal experiments. However, a useful

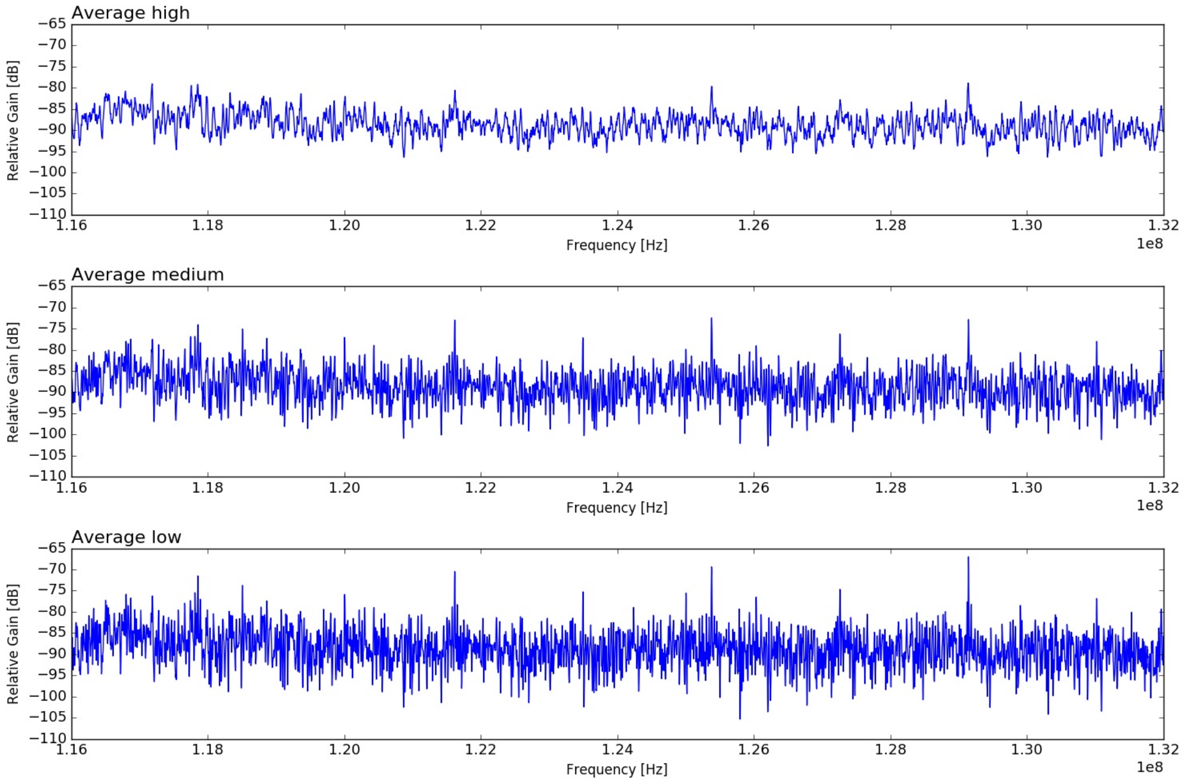

Figure 16. In-situ RFI measurements with high averaging (top), medium averaging (middle) and low averaging (bottom), considering a frequency range between 116 and 132 MHz.

future step in characterizing the long-term performance of the system will be to conduct an Allan variance analysis of the radiometric output. This test provides a direct measure of the stability and noise behavior of the full analog and digital signal chains over varying integration times. This provides a measure of the timescale beyond which systematics such as temperature drift, gain fluctuations, or ADC clock instabilities begin to dominate over thermal noise, thus limiting the effective integration time. Performing this test in controlled laboratory conditions will help determine whether the final prototype can achieve the ∼1000 h integrations required for global 21-cm signal detection and will inform both hardware improvements and calibration strategies before field deployment.

4.3. Comparison Between Simulations vs. Measurements

Here, we address the consistency between the simulation and measurement in terms of impedance match and gain, and assess the receiver performance in terms of sensitivity, noise floor, and linearity. To do this, we compared the S_{11} response of the blade antenna across five balun tuner heights (VNA temperature stability: 0.05 dB/°C). Table 11 summarizes the key quantities from the simulation and measurement, including the bandwidth defined by the −10dB threshold, frequency of minimum reflection, and peak return loss. Table 11 lists the numerical values of this comparison. A full comparison is presented in Figure 17.

At low balun heights (7.5 and 12.5 cm), the simulations and measurements agree well, with the reflection minimum shifting by only 4 and 1 MHz, respectively. As the balun height increased, the discrepancy became more noticeable. At 22.5, 32.5, and 45.5 cm, the measured S_{11} minima occur at lower frequencies than in the simulation by 6, 13, and 8 MHz, respectively.

The comparison between the simulated and measured S_{11} parameters shows both the frequency of minimum reflection and the bandwidth. The modest but consistent deviations between the simulations and measurements are likely due to the limitations of the simulation setup. The HFSS model used a reduced ground plane (1.3 × 1.0 m aluminum sheet) to limit the computational load, whereas the measured system included a 5 × 5 m wire mesh extension, which affected the impedance matching, particularly at the lower end of the frequency band.

In addition, the simulations assume ideal material properties and perfectly symmetrical structures, whereas a real antenna may exhibit small asymmetries owing to construction tolerances, feedline routing, and connector parasitics. Environmental factors, such as ground conductivity, dielectric constant of the soil, and nearby objects, may also influence the measured response. These effects result in frequency shifts of a few MHz in the location of the reflection minima, which are acceptable at this prototyping stage but will be addressed in future simulation campaigns that incorporate full site-specific boundary conditions.

5. Future Work

The results presented in this study establish a foundation for a low-frequency radiometric system capable of supporting future observational efforts targeting the global 21-cm signal and foreground removal strategies. Several lines of work are currently underway to improve the system's performance, expand its capabilities, and move toward field deployment at scientifically viable sites.

Table 11. S_{11} simulation vs measurement comparison for different balun heights

Concept	7.5cm	12.5cm	22.5cm	32.5cm	45.5cm
Simulation min. freq. @-10dB (MHz)	100	100	100	100	145
Measurement min. freq. @-10dB (MHz)	112	112	111	111	117
Simulation max. freq. @-10dB (MHz)	147	150	157	170	200
Measurement max. freq. @-10dB (MHz)	145	149	158	166	179
Simulation BW (bandwidth) (MHz)	47	50	57	70	55
Measurement BW (bandwidth) (MHz)	33	37	47	55	62
Simulation min. gain (dB)	-16.58	-17.98	-21.25	-28.54	-27.24
Measurement min. gain (dB)	-15.81	-16.50	-19.72	-41.91	-28.45
Simulation frequency @ min. gain (MHz)	122	123	130	139	169
Measurement frequency @ min. gain (MHz)	126	124	124	126	161

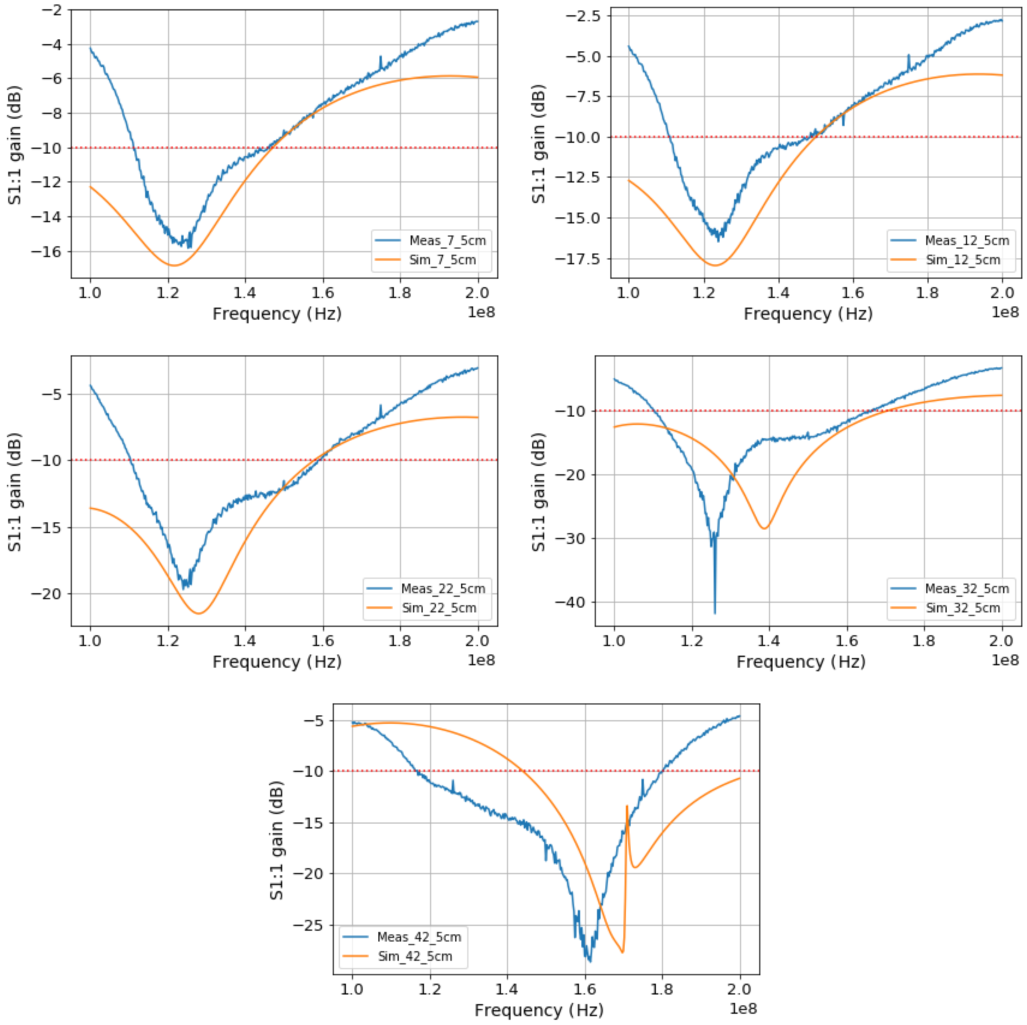

Figure 17. S_{11} simulation vs measurement plots for the blade antenna with balun tuner height @ 7.5 cm, 12.5 cm, 22.5 cm, 32.5 cm, and 42.5 cm.

We are developing novel software-optimized antenna designs (Restrepo et al., 2023) along with radio sky model validation of antenna chromaticity and Bayesian foreground models (Mora et al., in preparation).

Another immediate objective is to improve the absolute calibration accuracy of this system. This includes implementing a three-position switching scheme (antenna, load, and noise diode) to enable the calibration of the total power spectrum in physical temperature units, as well as tracking and correcting gain fluctuations over time. Laboratory tests of the switching mechanism and noise injection levels are currently being prepared.

We are developing improved analog front-end systems that incorporate high-selectivity bandpass filtering and enhanced gain flatness across the 100–200 MHz band. This design reduces out-of-band signal contamination and better matches the dynamic range constraints of the SDR receivers. New amplifiers with lower intrinsic noise temperatures and better impedance matching are being evaluated.

We are currently characterizing the RFI environment and antenna performance at potential observation sites with short-term deployments at remote locations in the Colombian Andes and Antarctica. Future deployments will focus on long-duration sky monitoring, interference analysis, and the assessment of diurnal stability and ionospheric variability.

From a software perspective, future development will include real-time data compression and RFI excision algorithms implemented on embedded systems to minimize storage requirements and support autonomous long-term operations. Real-time spectral averaging strategies, such as adaptive Savitzky–Golay filtering and time–frequency occupancy tracking, will be compared with standard post-processing pipelines.

In the longer term, this platform is intended to serve as the core for a field-deployable, calibrated radiometer capable of foreground characterization and model testing for global 21-cm signal detection. In particular, it will contribute to the design and validation of instruments suitable for operation in extreme environments, including high-altitude sites in Colombia and future campaigns on the Antarctic Peninsula.

6. Conclusions

We presented the design, simulation, implementation, and initial testing of a low-frequency radio telescope prototype developed to support future observations of the global 21-cm signal. The system combines a blade dipole antenna optimized for 100–200 MHz operation with a reconfigurable software-defined radio (SDR) receiver chain. Through a series of electromagnetic simulations, laboratory measurements, and in-situ tests, we evaluated the spectral response, sensitivity, and stability of the prototype in configurations relevant to global signal detection.

Simulations and measurements of the antenna reflection coefficient S_{11} across multiple balun tuner heights demonstrated good agreement, with frequency shifts between the modeled and measured resonances remaining below 15 MHz. SDR receiver tests showed that while all devices offered basic functionality across the desired band, the Ettus E310 provided the best performance in terms of noise floor, linearity, and dynamic range. Cascaded low-noise amplifiers reduced the system temperature to approximately 450 K, confirming the viability of this analog front-end configuration for moderate-sensitivity drift scan experiments.

The integrated system was deployed for initial data acquisition at a rural site in the Eastern Colombian Andes. Spectral measurements across the 100–212 MHz range confirmed broadband functionality and supported the preliminary evaluation of analog and digital filtering strategies. Although the system is not yet optimized for the detection of the 21-cm cosmological signal, its current configuration enables site testing, calibration experiments and foreground characterization.

Compared to established radiometers such as EDGES, SARAS, PRIZM, and BIGHORNS, this CANTAR prototype demonstrates broadly consistent performance in key areas such as impedance matching and system temperature, while introducing a novel digital backend architecture based on commercial software-defined radios (SDRs). For instance, our best-performing antenna configurations achieved simulated and measured S_{11} values below −25 dB over bandwidths of 50–70 MHz, which is comparable to the −15 to −20 dB targets reported for the EDGES high-band (Bowman et al., 2009) and SARAS 3 (Singh et al., 2018). Similarly, the prototype system temperature of 443–453 K using a dual-stage low-noise amplifier is within the 300–500 K range reported for BIGHORNS and PRIZM (Sokolowski et al., 2015; Philip et al., 2019).

Our choice to use SDRs rather than custom analog signal chains or digitizers introduced higher noise floors and greater spectral instability in devices such as the LimeNet Mini (noise floor −78 dB). This highlights the need to optimize the gain settings to prevent compression or quantization artifacts. Clock jitter, ADC resolution limits, and undocumented internal filtering further complicate the calibration process, which are less prominent in fixed-hardware systems.

Despite these limitations, our results show that with proper analog filtering and preamplifier design, SDR-based systems can meet the core sensitivity and linearity requirements for global 21-cm observations. Radiometric sensitivity estimates indicate that, under ideal conditions, the current system could reach sub-millikelvin thermal noise levels over 1 MHz bandwidths with 1000 hr of integration, suggesting that—despite remaining challenges in calibration and systematics control—it is thermally capable of detecting global 21-cm signals of cosmological origin.

This prototype marks an initial but necessary step toward the deployment of scientifically capable instrumentation for global 21-cm cosmology in Colombia and other countries. Continued development will focus on improving calibration, stability, and RFI mitigation while supporting training and capacity building for the national radio astronomy community.

GC received support from Proyecto CODI 2021-42970 Convocatoria Proyectos de Investigación Regionalización 2021, Vicerrectoría de Investigación, Universidad de Antioquia. OR thanks the Radio Astronomy Instrumentation Group of Universidad de Chile for generously sharing their ANSYS license for the electromagnetic simulations. The CASIRI Station and the Antarctic scientific expeditions were funded by Vicerrectoría de Investigación y Extensión VIE at Universidad Industrial de Santander and by MinCiencias with the project "Desarrollo de un arreglo interferométrico de Radio Telescopios para establecer una estación de Radio Astronomía de la UIS en el Páramo de Berlín (Santander)". contract No. 82527 CT ICETEX 2022-0723. The authors also express their gratitude to Programa Antártico Colombiano, Comisión Colombiana del Océano, Fuerza Aeroespacial Colombiana, Armada de Colombia, Instituto Antártico Chileno, Ejército de Chile, Armada de Chile, Fuerza Aérea de Chile for all their support that made our Antarctic Expeditions possible. The authors thank Jimena Giraldo for typesetting assistance.

REFERENCES

Barkana, R., & Loeb, A. 2005, ApJ, 626, 1, doi: 10.1086/429954

Bernardi, G., Zwart, J. T. L., Price, D., et al. 2016, MNRAS, 461, 2847, doi: 10.1093/mnras/stw1499

Bharadwaj, S., & Ali, S. S. 2004, MNRAS, 352, 142, doi: 10.1111/j.1365-2966.2004.07907.x

Bowman, J. D., Morales, M. F., & Hewitt, J. N. 2009, ApJ, 695, 183, doi: 10.1088/0004-637X/695/1/183

Bowman, J. D., Rogers, A. E. E., Monsalve, R. A., Mozdzen, T. J., & Mahesh, N. 2018, Natur, 555, 67, doi: 10.1038/nature25792

Cheng, C., Parsons, A. R., Kolopanis, M., et al. 2018, ApJ, 868, 26, doi: 10.3847/1538-4357/aae833

Costa, A. A., Landim, R. C. G., Wang, B., & Abdalla, E. 2018, EPJC, 78, 746, doi: 10.1140/epjc/s10052-018-6237-7

de Lera Acedo, E., de Villiers, D. I. L., Razavi-Ghods, N., et al. 2022, NatAs, 6, 984, doi: 10.1038/s41550-022-01709-9

DeBoer, D. R., Parsons, A. R., Aguirre, J. E., et al. 2017, PASP, 129, 045001, doi: 10.1088/1538-3873/129/974/045001

Facchinetti, G., Lopez-Honorez, L., Qin, Y., & Mesinger, A. 2024, JCAP, 2024, 005, doi: 10.1088/1475-7516/2024/01/005

Feng, W., Friedt, J.-M., & Wan, P. 2021, IEEE Transactions on Instrumentation and Measurement, 70, 1, doi: 10.1109/TIM.2021.3069805

Furlanetto, S. R., Oh, S. P., & Briggs, F. H. 2006, Physics Reports, 433, 181, doi: 10.1016/j.physrep.2006.08.002

Ghara, R., Zaroubi, S., Ciardi, B., et al. 2025, A&A, 699, A109, doi: 10.1051/0004-6361/202554163

Keller, R., Staufenbiel, B., & Aderhold, N. 2015, in 2015 1st URSI Atlantic Radio Science Conference (URSI AT-RASC), 1–1, doi: 10.1109/URSI-AT-RASC.2015.7303211

Monsalve, R. A., Rogers, A. E. E., Bowman, J. D., & Mozdzen, T. J. 2017, ApJ, 835, 49, doi: 10.3847/1538-4357/835/1/49

Monsalve, R. A., Altamirano, C., Bidula, V., et al. 2024, MNRAS, 530, 4125, doi: 10.1093/mnras/stae1138

Mozdzen, T. J., Bowman, J. D., Monsalve, R. A., & Rogers, A. E. E. 2016, MNRAS, 455, 3890, doi: 10.1093/mnras/stv2601

Philip, L., Abdurashidova, Z., Chiang, H. C., et al. 2019, Journal of Astronomical Instrumentation, 8, 1950004, doi: 10.1142/S2251171719500041

Price, D. C., Greenhill, L. J., Fialkov, A., et al. 2018, MNRAS, 478, 4193, doi: 10.1093/mnras/sty1244

Ragoomundun, N., & Beeharry, G. K. 2019, ExA, 47, 313, doi: 10.1007/s10686-019-09629-9

Restrepo, O. A., Lucero, F. I., Chaparro, G., et al. 2023, JAI, 12, 2350005, doi: 10.1142/S2251171723500058

Restrepo, O. A., Lucero, F. I., Molina, R., et al. 2020, BAAA, 61C, 65

Rogers, A. 2012, EDGES Group Memo 087, https://www.haystack.mit.edu/wp-content/uploads/2020/07/memo_EDGES_087.pdf

Singh, S., Subrahmanyan, R., Shankar, N. U., et al. 2018, ExA, 45, 269, doi: 10.1007/s10686-018-9584-3

Sokolowski, M., Tremblay, S. E., Wayth, R. B., et al. 2015, PASA, 32, e004, doi: 10.1017/pasa.2015.3

Vacaliuc, B., Oxley, P., Fields, D., Kurtz, D. S., & Leech, M. 2011, in Annual meeting of the Society of Amateur Radio Astronomers, Oak Ridge National Laboratory (ORNL). https://www.osti.gov/biblio/1074425